

Article

Improved Bathymetry Estimation Using Satellite Altimetry-Derived Gravity Anomalies and Machine Learning in the East Sea

Kwang Bae Kim ¹ , Jisung Kim ^{2,*}  and Hong Sik Yun ³ 

¹ Department of Civil, Architectural and Environmental System Engineering, Sungkyunkwan University, 2066 Seobu-ro, Jangan-gu, Suwon 16419, Republic of Korea; kbkim929@skku.edu

² School of Geography, Faculty of Environment, University of Leeds, Woodhouse Lane, Leeds LS2 9JT, UK

³ Department of Interdisciplinary Program in Crisis, Disaster and Risk Management, Sungkyunkwan University, 2066 Seobu-ro, Jangan-gu, Suwon 16419, Republic of Korea; yoonhs@skku.edu

* Correspondence: gyjki@leeds.ac.uk

Abstract: This study aims to improve the accuracy of bathymetry predicted by gravity-geologic method (GGM) using the optimal machine learning model selected from machine learning techniques. In this study, several machine learning techniques were utilized to determine the optimal model from the performance of depth and gravity anomalies. In addition, a tuning density contrast calculated from satellite altimetry-derived free-air gravity anomalies (FAGAs) was applied to estimate enhanced bathymetry. By comparison with shipborne depth, the accuracy of the bathymetry estimated by using satellite altimetry-derived FAGAs and machine learning was evaluated. The findings reveal that the bathymetry predicted by the optimal machine learning using the Gaussian process regression and the GGM with a tuning density contrast can enhance the accuracy of 82.64 m, showing an improvement of 67.40% in the RMSE at shipborne depth measurements. Although the tuning density is larger than 1.67 g/cm³, bathymetry using satellite altimetry-derived FAGAs and machine learning can be effectively improved with higher accuracy.

Keywords: optimal machine learning; gravity anomalies; density contrast; east sea



Citation: Kim, K.B.; Kim, J.; Yun, H.S.

Improved Bathymetry Estimation Using Satellite Altimetry-Derived Gravity Anomalies and Machine Learning in the East Sea. *J. Mar. Sci. Eng.* **2024**, *12*, 1520. <https://doi.org/10.3390/jmse12091520>

Academic Editor: Chung-yen Kuo

Received: 12 August 2024

Revised: 29 August 2024

Accepted: 1 September 2024

Published: 2 September 2024



Copyright: © 2024 by the authors. Licensee MDPI, Basel, Switzerland. This article is an open access article distributed under the terms and conditions of the Creative Commons Attribution (CC BY) license (<https://creativecommons.org/licenses/by/4.0/>).

1. Introduction

Because bathymetry is crucial in understanding the Earth's shape, seafloor evolution, marine resource exploration, marine navigation, and marine environment monitoring, relevant research is continuously being conducted to estimate accurate bathymetry as technology advances. Several satellite radar altimeters have provided accurate sea surface topography by measuring the distance between the satellite and the sea surface.

The sea surface topography derived from the distance measurements of the satellite radar altimeters between the satellite and the sea surface can be recovered to global marine altimetry-derived gravity anomalies, which have a more uniform and denser coverage than the ship tracks. The three main satellite altimetry-derived geophysical parameters, such as marine geoid, marine gravity anomalies, and bathymetry, are correlated with the undulations of the crustal density variations under the seafloor [1]. Satellite altimetry-derived free-air gravity anomalies (FAGAs) are critical in generating accurate bathymetry maps by filling large gaps between the bathymetry data on the shipborne tracks using the topographic effects in the off-tracks in the ocean [2,3].

Several studies about bathymetry predictions using the gravity-geologic method (GGM) from the satellite altimetry-derived FAGAs and the density contrast between seawater and the ocean bedrock were carried out. Roman (1999) [4] adapted GGM to estimate bedrock elevation beneath unconsolidated materials for bathymetric determinations in the Barents Sea and the waters around Greenland. Checkpoints with the GGM and the

downward continuation method were applied to generate enhanced bathymetry using a density contrast of 10.25 g/cm^3 in the Ulleung basin in the East Sea [2]. Kim and Lee (2015) [5] computed bathymetric change before and after the 2011 Tohoku Earthquake using a density contrast of 17.04 g/cm^3 in the Japan Trench. An improved bathymetry model in the Gulf of Guinea was estimated using an optimal density contrast of 8.0 g/cm^3 determined by the GGM [6]. They compared the accuracy of the inversion bathymetry with the new optimal density contrast, which is computed by considering the seafloor topography in each of the three subregions.

Satellite-derived bathymetry predictions in shallow waters using GGM were made on the western coast of Korea. The enhanced bathymetry predictions in shallow waters around coastal areas in western Korea were implemented by combining shipborne multi-beam data, satellite altimetry-derived FAGAs, and airborne bathymetric LiDAR data [7]. The satellite-derived bathymetry estimated by combining multi-beam depth and airborne bathymetric LiDAR was remarkably enhanced in shallow waters in comparison with bathymetry predicted by only multi-beam depth data.

Several studies adopted various machine learning-based regression models to estimate seafloor topography, confirming that machine learning-based regression models effectively estimate bathymetry [8–14]. Alevizos (2020) used hyperspectral imaging and machine learning to estimate shallow-depth bathymetry and proved its accuracy using ground truth data [8]. Tonion et al. (2020) [9] demonstrated that support vector machines (SVMs) and random forests (RFs) effectively estimate bathymetry at shallow depths. On the other hand, Surisetty et al. (2021) [10] estimated the bathymetry using an ensemble model. Although these study areas differ, these studies are significant because they all estimated the bathymetry using machine learning-based methods. Nevertheless, because different machine learning methods were applied, there is a limitation in that it is impossible to know which method is optimal for estimating bathymetry.

To address this limitation, further studies comparing various machine-learning methods in bathymetry estimation [11–14] were conducted and recommended. For instance, Eugenio et al. (2022) [11] verified through Root Mean Square Error (RMSE) and coefficient of determination (R^2) that the performance of subspace K-Nearest Neighbor (KNN) and bagged trees is superior to other machine learning methods in estimating bathymetry. Ashphaq et al. (2022) [12] also demonstrated that the Gaussian process regression (GPR) method is superior to other machine learning methods through RMSE, Mean Absolute Error (MAE), and coefficient of determination. Zhou et al. (2023) [13] also compared the performance of each machine learning model through RMSE, MAE, error distribution, and coefficient of determination. Lastly, Cheng et al. (2023) [14] differentiated the bathymetry estimation performance of each machine learning-based regression model using RMSE and MAE.

The implications of these prior studies are significant. First, the appropriate regression model for estimating bathymetry varies for each region due to regional characteristics. For example, in this study area of Eugenio et al. (2022) [11], bagged tree is the most optimal learning model, but in this study area of Ashphaq et al. (2022) [12], the GPR method is the most appropriate learning model. Therefore, it is necessary to find an optimal learning model according to this study area and to apply the learning model. Second, RMSE, MAE, and coefficient of determination are used to find an optimal learning model. Therefore, considering previous studies, it can be inferred that the approach to finding the optimal learning model using RMSE, MAE, mean square error (MSE), and coefficient of determination is reasonable.

Another limitation of the above-mentioned studies [8–14] is that their target areas are shallow (within 100 m). Therefore, there are limitations in estimating bathymetry at deep depths using methods for estimating bathymetry at shallow depths. Hence, studies applying machine learning to deep-depth bathymetry were conducted [15–17]. Annan et al. (2022) [15] estimated the bathymetry using Convolution Neural Network (CNN), where CNN was utilized to merge these three gravity signals, which are gravity anomalies,

vertical gravity anomaly gradient, and vertical deflections, to enhance the bathymetry of the Gulf of Guinea. Li et al. (2023) [17] used a fully connected deep neural network (FC-DNN) to estimate bathymetry of the South China Sea. They used it to synthesize gravity anomaly (GA), vertical gravity gradient anomaly (VGG), and deflection of vertical (DOV). Their study was based on control points and checkpoints as a verification method, but this method is not suitable for the current study because it differs from the regression this study intends to perform. However, both studies [15,16] did not compare performance among other machine learning methods they used, so it is not clear whether the machine learning model is the optimal model they used. In Kim et al. (2023) [17], the performances of machine learning models in deep water were compared, showing the progress of bathymetry estimation research compared to other research about shallow water [8–14] and deep water [15,16]. Consequently, this study intended to apply the machine learning models presented in previous studies to a pilot area, analyze their performances, and estimate the bathymetry using the optimal model.

In summary, this study has similarities and advances from previous studies. The similarity to previous studies is that the optimal artificial intelligence (AI) model for bathymetry estimation in the target area is unknown; therefore, the optimal model must be selected through RMSE, MSE, MAE, and coefficient of determination. On the other hand, since most of the previous studies were conducted at shallow depths, there is a gap in the feasibility of applying machine learning to deep-water bathymetry estimation. In this respect, the novelty of this study is that machine learning models are applied to deep-depth bathymetry estimation, and their effectiveness is proven.

This study estimated bathymetry around the Yamato basin in the East Sea using the optimal machine learning model and the gravity-geologic method (GGM) with a tuning density contrast. To improve the accuracy of the estimated bathymetry, the optimal machine learning model with the best performance was selected by assessing the shipborne depth and gravity anomalies predicted from various machine learning models. Additionally, a tuning density contrast determined using downward continuation of gravity anomalies was applied to effectively predict bathymetry. We evaluated the accuracy of bathymetry in this study area in comparison with shipborne bathymetry as well as the global bathymetry, such as the Earth topographical database 1 (ETOPO1) [18].

2. Materials and Methods

2.1. Data Set

The East Sea comprises three sub-basins, which are a mature back-arc basin behind Japan island arcs in the northwestern Pacific, in Figure 1. In comparison with the Japan basin, which is a deep (>3000 m) and large back-arc basin located in the northeastern part of the East Sea, the Yamato basin is a relatively shallow (<3000 m) back-arc basin, similarly to the Ulleung basin [19]. This study area (136.7°–139.7° E, 38.9°–41.4° N) selected is the red box in the location map in Figure 1. The bathymetry as a background from ETOPO1 is also depicted in Figure 1. The spatial resolution and accuracy of ETOPO1 are 1 arc-minute and 10 m, respectively [18]. The water depth in the Yamato basin in the East Sea is less than 3000 m.

Figure 2a portrays the ETOPO1 bathymetry with superimposed 108,056 shipborne measurements (including depth and gravity anomalies) locations provided by the National Centers for Environmental Information (NCEI) and the National Oceanic and Atmospheric Administration (NOAA). About 72,045 control points and 36,011 checkpoints accounting for the 108,056 NCEI shipborne measurements were selected to determine a tuning density contrast by checkpoint using GGM. The depths from ETOPO1 in this study area ranged from −3755.4 to 0.0 m, as illustrated in the background in Figure 2a. The 1 arc-minute satellite altimetry-derived FAGAs [20] obtained from Scripps Institution of Oceanography (SIO), University of California, San Diego, used to improve bathymetry in this study area are presented in Figure 2b. The spatial resolution and accuracy of satellite altimetry-derived FAGAs are 1 arc-minute and 2 mGal (1 mGal = 1×10^{-5} m/s²) [20]. Attributes

(AR, AM, ASD, and AU) listed for subsequent maps represent amplitude range (minimum and maximum values), amplitude mean, amplitude standard deviation, and amplitude unit, respectively.

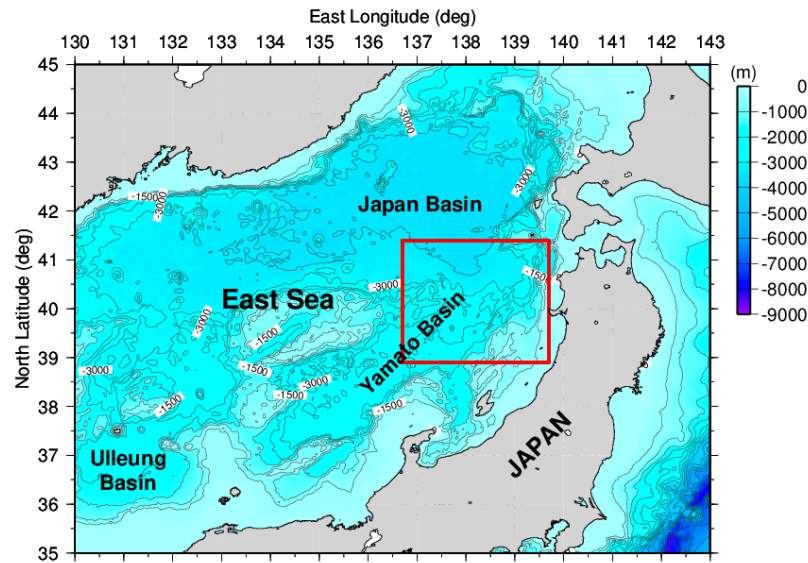


Figure 1. Location map. The red box represents this study area (136.7°–139.7° E, 38.9°–41.4° N).

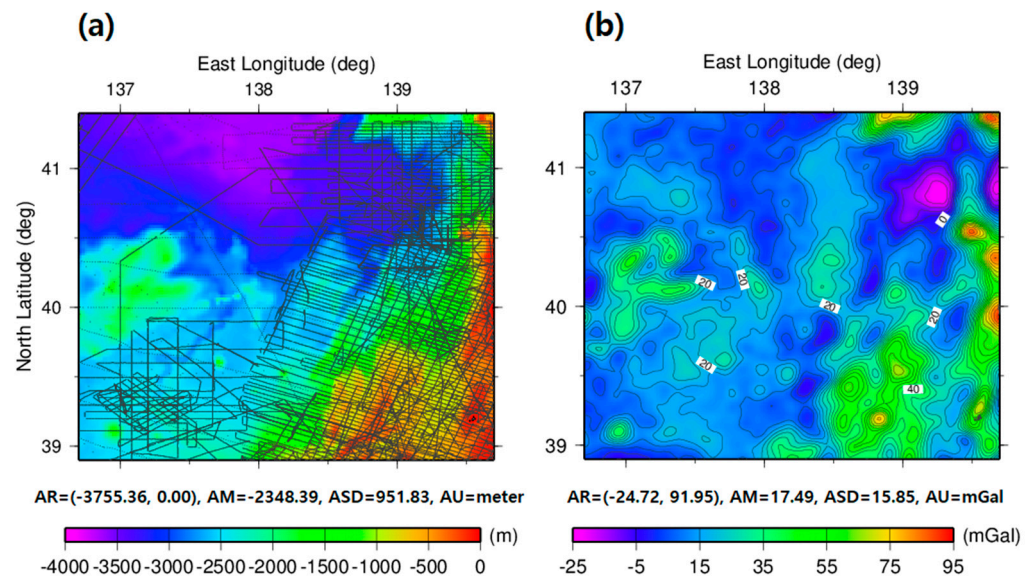


Figure 2. (a) The ETOPO1 bathymetry with superimposed shipborne track locations by the NCEI and (b) satellite altimetry-derived FAGAs in this study area.

2.2. Methodology

2.2.1. Depth and Gravity Anomalies Predictions Using Optimal Machine Learning

This study compared the performances of machine learning methods to estimate seafloor topography and bathymetry by applying machine learning to shipborne depth and gravity anomalies.

Machine learning models suitable for estimating bathymetry are highlighted in previous research. Representative examples are artificial neural networks (ANNs), SVM, RF, and GPR. ANN is an artificial neural network constructed using multiple perceptrons. Depending on its structure, such as CNN [15], FC-DNN [16], and recurrent neural network (RNN) [21], it can be used to estimate bathymetry in various ways. SVM is a non-parametric method and is based on supervised classification [22]. This was developed to classify two

different classes on a hyperplane with the maximum margin between the two classes [23]. Therefore, the kernel that expresses the phenomenon on the hyperplane is vital to the SVM [9]. RF was developed as a kind of decision tree [24]. Representative RF models are the bagging tree [25] and the boosting tree [26]. The ensemble model overcomes the limitations of each method by combining bagging trees and boosting trees [27]. Ensemble models have excellent performance in bathymetry estimation [17]. Lastly, GPR is quite similar to SVM. Such as SVM, GPR is a supervised classification and can perform differently depending on the kernel type [12].

In estimating bathymetry, because various machine-learning models produce various results, it is necessary to select and use the machine-learning model with the best performance. Since it has already been proven in previous studies that RMSE, MAE, and coefficient of determination indicate the superiority of the model [11–14,17], adopting the optimal model using RMSE, MAE, MSE, and coefficient of determination is recommended for this study as well. The formulas for RMSE, MAE, MSE, and coefficient of determination are as follows:

$$RMSE = \sqrt{\frac{\sum_{i=1}^n (x_i - y_i)^2}{n}} \tag{1}$$

$$MAE = \frac{1}{n} \sum_{i=1}^n |x_i - y_i| \tag{2}$$

$$MSE = \frac{1}{n} \sum_{i=1}^n (x_i - y_i)^2 \tag{3}$$

$$R^2 = 1 - \frac{MSE(predicted)}{MSE(observed)} \tag{4}$$

where x_i is the predicted value; y_i is the observed value; n is the number of observed points.

GPR is a nonlinear supervised classification-based regression model [12] and has various characteristics. First, GPR is based on a Gaussian probability distribution [28]. When there is only one variable, the Gaussian probability distribution function (PDF) is equal to Equation (5), and when there are two or more variables, such as in this study, the D-dimensional multivariate distribution model is equal to Equation (6) [29].

$$P_X(x) = \frac{1}{\sqrt{2\pi}\sigma} \exp\left(-\frac{(x - \mu)^2}{2\sigma^2}\right) \tag{5}$$

$$N(x|\mu, \Sigma) = \frac{1}{(2\pi)^{D/2} |\Sigma|^{1/2}} \exp\left[-\frac{1}{2} x - \mu^T \Sigma^{-1} (x - \mu)\right], \tag{6}$$

where X is a random variable and x is the real argument. X is usually represented by $P_X(x) \sim N(\mu, \sigma^2)$ [28]. D is the number of the dimensionality, $\mu = E[x] \in \mathbb{R}^D$ is the mean vector, and $\Sigma = \text{cov}[x]$ is the $D \times D$ covariance matrix [28]. The Σ is a symmetric matrix storing the pairwise covariance of all jointly modeled random variables, with $\Sigma_{ij} = \text{cov}(y_i, y_j)$ as its (i, j) element [28]. Here, $\Sigma_{ij} = \text{cov}(y_i, y_j)$ represents the kernel. Using this, the exponential kernel function can be expressed as Equation (7) [30].

$$k_{exp}(x_i, x_j) = s^2 \exp\left(-\frac{r}{l}\right), \tag{7}$$

where s and l are again the scale factor and length scale hyperparameter. r is the Euclidean distance between x_i and x_j .

The GPR model has various advantages and disadvantages. The advantages are that probabilistic prediction is used in data interpolation; the confidence interval is determined according to the Gaussian model; various results can be derived depending on the kernel; and the kernels are widely known [12]. Contrarily, the disadvantages of GPR are that the accuracy of the prediction results varies depending on the distribution of observations, and when there are many variables, the calculation is complicated, and efficiency is reduced [12].

Nonetheless, the GPR model is considered since only latitude, longitude, and observed value are the variables in this study.

2.2.2. GGM Bathymetry Predictions

This research utilized the shipborne depth and gravity anomalies predicted by the optimal machine learning model with the best performance to estimate bathymetry by the GGM. Figure 3 reveals this study’s flowchart on the GGM bathymetry estimation using depth and gravity predicted from the optimal machine learning model.

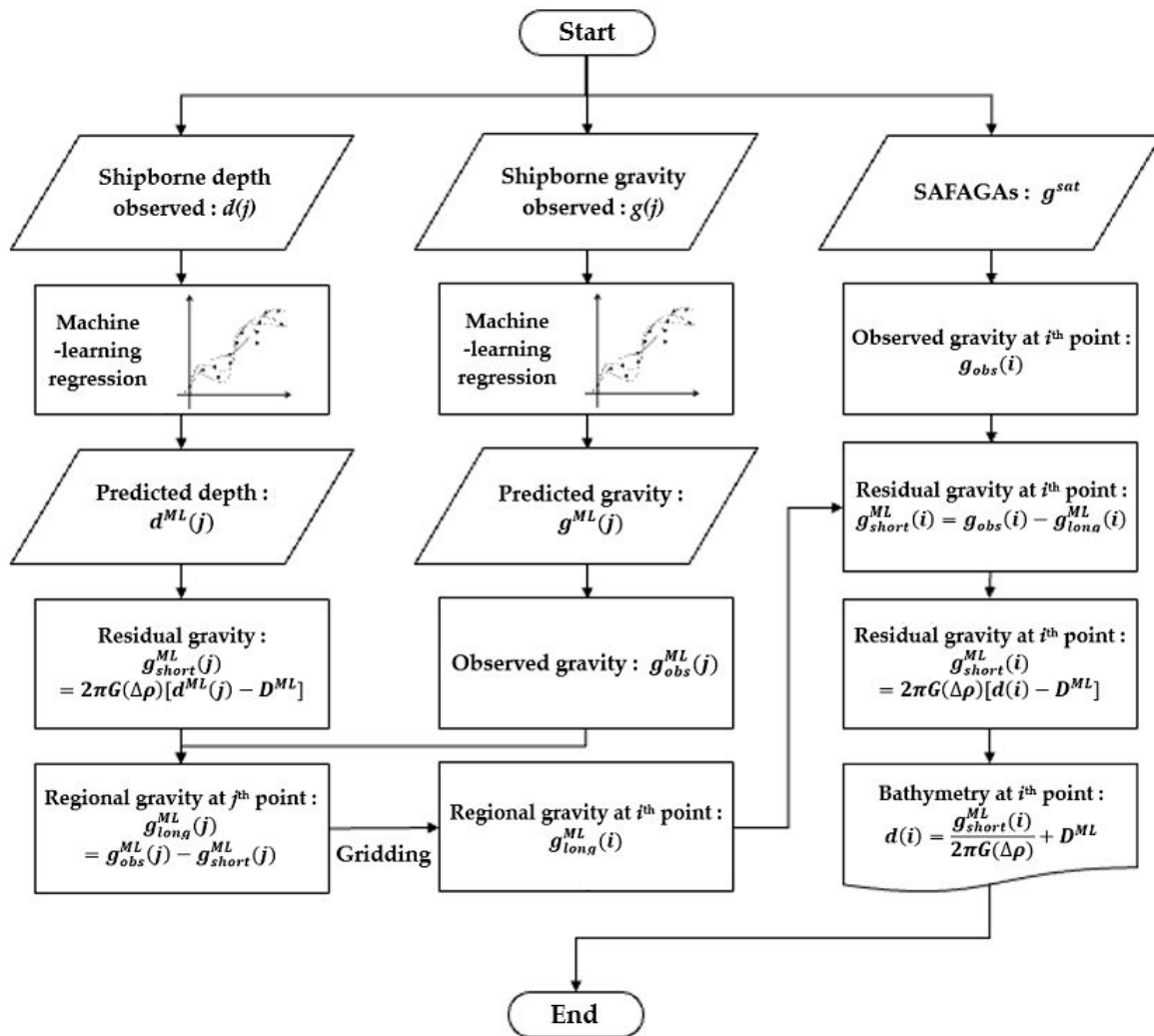


Figure 3. Bathymetry estimation process using machine learning.

The GGM to effectively generate bathymetry was adapted in marine environments using FAGAs and depth measurements instead of Bouguer gravity anomalies (BGAs) and borehole measurements [2,3]. In addition, a single tuning density contrast determined by the downward continuation method was employed to improve bathymetry in this study.

The observed gravity (g_{obs}) is composed of the residual gravity (g_{short}) of a short-wavelength part and the regional gravity (g_{long}) of a long-wavelength part.

Firstly, for the depth [$d^{ML}(j)$] predicted from shipborne depth observed values [$d(j)$] the optimal machine learning model was used to generate the residual gravity [$g_{short}^{ML}(j)$] in the shorter wavelength effect from a simple Bouguer slab formula at the control points, j .

$$g_{short}^{ML}(j) = 2\pi G(\Delta\rho) [d^{ML}(j) - D^{ML}] \tag{8}$$

where G is the gravitational constant, $6.672 \times 10^{-8} \text{ cm}^3/\text{g}\cdot\text{s}^2$; $\Delta\rho$ is the density contrast between seawater and the ocean bedrock (g/cm^3); D^{ML} is the deepest depth at a reference datum (m) using the optimal machine learning model at measured point j .

Secondly, the residual gravity $[g_{short}^{ML}(j)]$ is eliminated from the observed gravity $[g_{obs}^{ML}(j)]$ predicted from shipborne gravity observed values $[g(j)]$ using the optimal machine learning model to calculate the regional gravity $g_{long}^{ML}(j)$ that represents the longer wavelength effect at the control points of measured depth j .

$$g_{long}^{ML}(j) = g_{obs}^{ML}(j) - g_{short}^{ML}(j) \tag{9}$$

Thirdly, the regional gravity $g_{long}^{ML}(i)$ at the points of unmeasured depth, i can be calculated by interpolating as a grid by minimum curvature method using the regional gravity $g_{long}^{ML}(j)$ at the control points of measured depth j . The residual gravity field $g_{short}^{ML}(i)$ for predicting the depth between the sea surface and the seafloor bedrock at the sites of unmeasured depth i was estimated by eliminating the regional gravity using the following equation:

$$g_{short}^{ML}(i) = g_{obs}(i) - g_{long}^{ML}(i) \tag{10}$$

The generated residual gravity, $g_{short}^{ML}(i)$, at the points of unmeasured depth i , can be represented as

$$g_{short}^{ML}(i) = 2\pi G(\Delta\rho)(d(i) - D^{ML}) \tag{11}$$

Finally, by rearranging Equation (11), the depth of the seafloor bedrock above the reference where the seafloor bedrock depths are unmeasured at site i can be predicted, as shown in Equation (12) below.

$$d(i) = \frac{g_{short}^{ML}(i)}{2\pi G(\Delta\rho)} + D^{ML} \tag{12}$$

Moreover, a tuning density contrast between seawater and the ocean bedrock was determined to predict accurate bathymetry. The downward continuation method can be applied to select a single tuning density contrast within the trade-off diagram determined by the GGM in this study. Upward continuation in the frequency domain from the gravity field at $z = h_1$ plane to $z = h_2$ plane in the Fourier domain can be expressed as [31]:

$$G_{h_2}(u, v) = e^{-2\pi kd} G_{h_1}(u, v) \tag{13}$$

where $G_{h_1}(u, v)$ and $G_{h_2}(u, v)$ are the two-dimensional Fourier transform of the gravity field at h_1 and h_2 , respectively; u and v are the frequencies for x and y directions, respectively; $k = \sqrt{u^2 + v^2}$; and $d = h_2 - h_1$.

Downward continuation of the gravity field in the Fourier transform from $z = h_2$ to $z = h_1$ plane by inverting Equation (13) as:

$$G_{h_1}(u, v) = e^{2\pi kd} G_{h_2}(u, v) \tag{14}$$

The downward continued gravity field was identified in each downward continued level from the sea surface to the ocean bottom of the deepest point by applying the Gaussian filter in Equation (15):

$$\bar{G}(u, v) = F(u, v)G(u, v)e^{2\pi kd} \tag{15}$$

where $\bar{G}(u, v)$ is the downward continued gravity field; $F(u, v)$ is a Gaussian filter; $G(u, v)$ is the original gravity field; and d is the distance of the downward continuation.

This study determined a tuning density contrast by the downward continuation method using satellite altimetry-derived FAGAs in the deepest ocean bedrock. The density contrast at point i of every downward continued level can be calculated by multiplying the

gravity ratio at the point i of each downward continued level and the sea surface level by 1.03 g/cm^3 [32].

3. Results and Discussions

As explained in the methods, the RMSE, R^2 , MSE, and MAE in the validation set and a test set of depth and gravity anomaly of 108,056 shipborne measurements denoted as black dots in Figure 2a were compared to determine the optimal machine learning model in this study. The smaller the RMSE, MSE, and MAE are, the better the performance becomes, with higher R^2 also yielding better performance. The shipborne depth and gravity anomaly data were divided into validation and test data in the ratios of 90:10, and the model with the best performance was selected in this research. A total of 97,250 validation data and 10,806 test data in shipborne depth and shipborne gravity anomalies were analyzed for the 90:10 ratio.

As a result of the regression performance of the depth and gravity anomaly in this study using various machine learning methods, the exponential GPR model exhibited the best performance from the comparative analysis of the validation and test data results for the ratios of 90:10, as demonstrated in Tables 1 and 2. In both cases, SVM, artificial neural networks, and boosting tree methods had poor performance. When exponential GPR was applied to the regression of the shipborne depth, the RMSE was approximately 24.00 m, the coefficient of determination was 1.00, and the MAE was within 7.00 m. These results are reliable because they are similar in the validation and the test. Even in the case of the shipborne gravity anomaly, the exponential GPR is superior to the others. In this case, the RMSE was about 7.00 mGal, the MAE was all below 2.00 mGal, and the coefficient of determination was above 0.90. Therefore, estimating the bathymetry using the predicted depth and gravity anomaly from the exponential GPR in this study is essential.

Table 1. Comparative analysis of shipborne depth prediction performance for each machine learning model with a ratio of 90:10.

Model	Validation				Test				
	RMSE (m)	R^2	MSE (m ²)	MAE (m)	RMSE (m)	R^2	MSE (m ²)	MAE (m)	
Neural Network	Triple Layer Neural Network	200.09	0.96	40,037.00	141.33	232.19	0.95	53,913.00	162.04
SVM	Optimization SVM	384.13	0.85	147,560.00	282.77	399.2	0.84	159,360.00	287.23
	Linear SVM	506.30	0.75	256,340.00	380.85	513.73	0.74	263,910.00	382.00
	Quadratic SVM	436.98	0.81	190,950.00	333.38	440.75	0.81	194,260.00	333.84
	Cubic SVM	422.30	0.82	178,330.00	307.75	469.16	0.78	220,120.00	326.96
	Fine Gaussian SVM	113.65	0.99	12,916.00	86.44	115.28	0.99	13,289.00	86.78
	Coarse Gaussian SVM	202.51	0.96	41,012.00	146.08	203.03	0.96	41,219.00	145.06
Decision Tree	Optimization Tree	49.28	1.00	2428.20	28.65	46.42	1.00	2154.80	27.32
	Fine Tree	49.32	1.00	2432.70	28.59	46.59	1.00	2170.70	27.31
	Medium Tree	56.08	1.00	3144.80	31.55	53.54	1.00	2866.20	29.85
	Coarse Tree	77.33	0.99	5979.50	43.68	70.91	0.99	5028.80	39.46
GPR	Rational Quadratic GPR	23.52	1.00	552.94	8.56	25.49	1.00	649.63	9.77
	Squared Exponential GPR	57.30	1.00	3283.60	33.97	73.36	0.99	5382.10	44.43
	Matern 5/2 GPR	30.30	1.00	918.35	14.30	32.45	1.00	1053.20	15.46
	Exponential GPR	21.89	1.00	479.36	6.73	23.27	1.00	541.35	6.15
Ensemble	Boosting Tree	210.42	0.96	44,276.00	169.54	209.95	0.96	44,078.00	168.86
	Bagging Tree	39.06	1.00	1525.70	21.97	37.85	1.00	1432.40	21.10
	Optimization Tree	36.10	1.00	1366.10	21.11	35.95	1.00	1292.70	20.44

Table 2. Comparative analysis of shipborne gravity anomaly prediction performance for each machine learning model with ratio of 90:10.

	Model	Validation				Test			
		RMSE (mGal)	R ²	MSE (mGal ²)	MAE (mGal)	RMSE (mGal)	R ²	MSE (mGal ²)	MAE (mGal)
Neural Network	Triple Layer Neural Network	12.53	0.66	157.06	7.11	12.57	0.68	157.96	6.92
SVM	Optimization SVM	21.63	0.00	467.68	15.71	22.21	0.00	493.48	15.85
	Linear SVM	19.78	0.16	391.35	13.63	20.47	0.15	491.10	13.79
	Quadratic SVM	19.54	0.18	381.65	12.89	20.23	0.17	609.05	13.07
	Cubic SVM	19.14	0.22	366.19	12.55	19.71	0.21	388.34	12.65
	Fine Gaussian SVM	10.99	0.74	120.74	3.98	11.95	0.71	142.81	4.12
	Medium Gaussian SVM	15.35	0.50	235.52	8.46	16.09	0.48	258.88	8.58
	Coarse Gaussian SVM	18.96	0.23	359.37	12.34	19.57	0.22	382.90	12.43
Decision Tree	Optimization Tree	7.35	0.88	54.00	1.92	9.03	0.83	81.52	1.98
	Fine Tree	7.36	0.88	54.23	1.90	9.04	0.83	81.63	1.97
	Medium Tree	7.64	0.88	58.42	2.21	8.30	0.86	68.90	2.18
	Coarse Tree	8.65	0.84	74.79	2.95	9.15	0.83	83.70	2.86
GPR	Rational Quadratic GPR	5.90	0.93	34.75	1.37	9.03	0.83	81.51	2.58
	Squared Exponential GPR	8.64	0.84	74.71	2.67	9.30	0.82	86.48	2.84
	Matern 5/2 GPR	7.97	0.86	63.47	2.23	7.89	0.87	62.20	2.05
	Exponential GPR	5.00	0.95	25.03	1.12	6.52	0.91	42.50	1.60
Ensemble	Boosting Tree	13.63	0.60	185.70	7.79	14.37	0.58	206.39	7.99
	Bagging Tree	6.63	0.91	43.95	1.78	7.38	0.89	54.53	1.80
	Optimization Tree	6.61	0.91	43.68	1.71	7.31	0.89	53.37	1.71

The performance of the machine learning model using the exponential GPR can also be measured through the residual, which is the difference between predicted and observed values in both depth and gravity anomaly. Because the observed values are the most probable values, observed values are regarded as true values in this study. Figure 4 illustrates the distributions of the residuals of depth and the gravity anomaly, respectively. In addition, Figure 5 displays the histograms of the residuals of the depth and the gravity anomaly, respectively.

The performances of the machine learning models considered in this study are quite similar to those of previous studies. According to previous studies [9,11–13], GPR has shown the best performance, followed by ensemble and decision tree at a similar level. Next, artificial neural networks are excellent, while SVM has the worst performance [9,11–13]. Of course, the performance of these models varies depending on depth, but this is not significant [8,13,14]. Therefore, this suggests that the models applied for shallow depth bathymetry estimation are also effective for deep depth bathymetry estimation, making the results derived from this study.

Unfortunately, however, the cause of the performance is unclear. Although various studies have analyzed the performance of machine learning models [8–14], it is difficult to find in-depth cause analysis beyond general observation results. Performance has been found to vary depending on depth [8,13,14] and may also vary depending on the kernel used [8]. Unfortunately, this study also could not identify the cause of the performance difference.

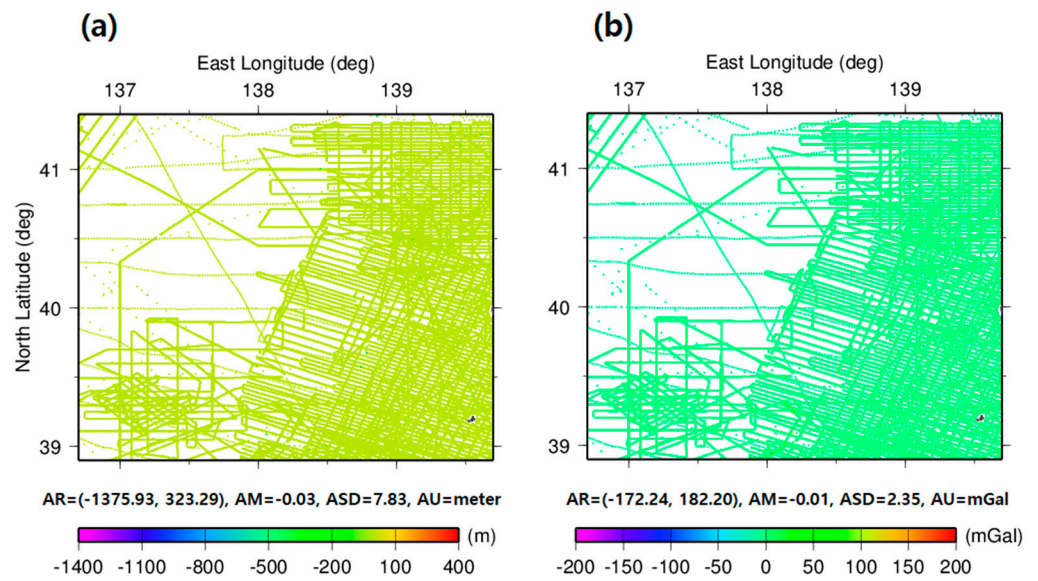


Figure 4. (a) The residuals of the depth between observed and predicted values and (b) the residuals of the gravity anomaly between observed and predicted values.

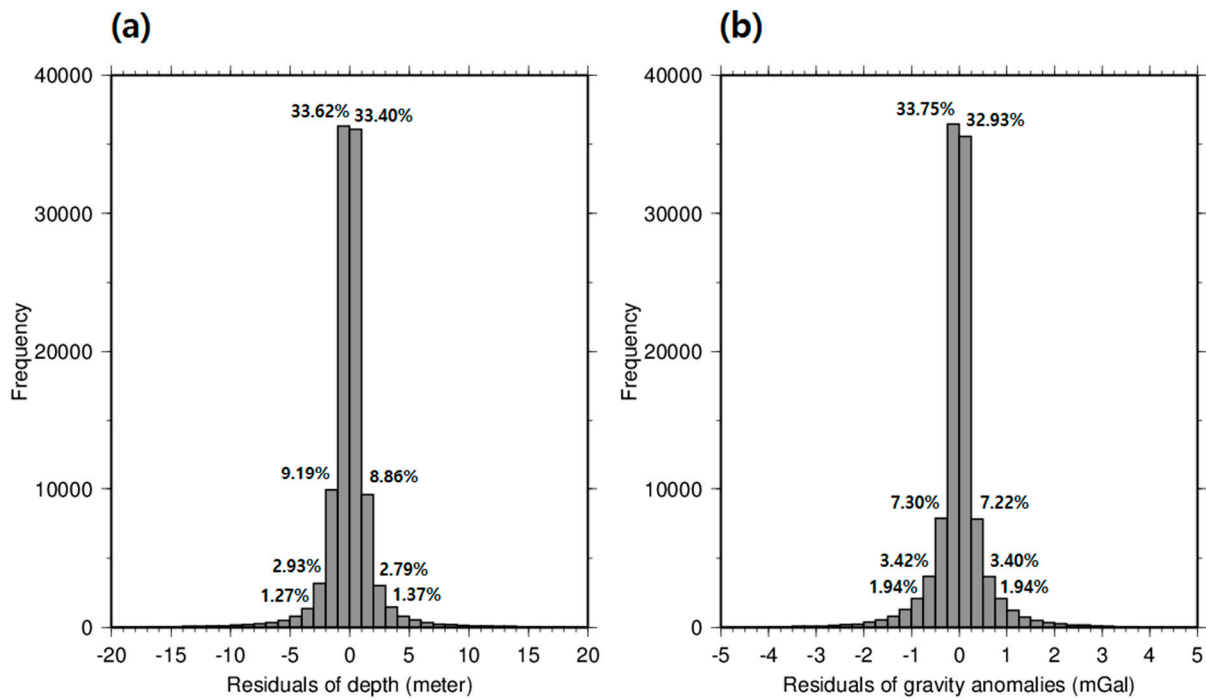


Figure 5. (a) The histogram of the residuals of the depth between observed and predicted values and (b) the histogram of the residuals of the gravity anomaly between observed and predicted values.

The residuals of the depth predicted by using the exponential GPR were a minimum of -1375.93 m and a maximum of 323.29 m, with an average of -0.03 m and a standard deviation of 7.83 m. Accordingly, the distribution of the residuals of the depth in the 95% confidence interval can range from -15.35 m to 15.35 m. Likewise, the residual of gravity anomaly predicted using the exponential GPR was a minimum of -172.24 mGal and a maximum of 182.20 mGal, with an average of -0.01 mGal and a standard deviation of 2.35 mGal. Accordingly, the distribution of residuals of the depth in the 95% confidence interval can range from -4.61 mGal to 4.61 mGal.

Figure 5 details the histograms of the residuals of depth and gravity anomalies predicted using the exponential GPR. From the histograms of the residuals of the depth and the gravity anomalies between observed and predicted values in Figure 5, 94.95% of the residuals of depth were distributed between -5.0 and 5.0 m, and the 95.69% of the residuals of gravity anomalies were distributed between -1.5 and 1.5 mGal.

This research utilized the 108,056 NCEI shipborne data, including depth and gravity anomalies, to estimate the improved bathymetry from topographic effects extracted from FAGAs and predicted the depth and gravity anomalies using the exponential GPR.

To meet the checkpoints of the GGM, the NCEI shipborne data in this study area were divided into 72,045 control points and 36,011 checkpoints, as detailed in Figure 2a, respectively, to calculate satellite-derived bathymetry estimation error by the GGM. Every third point of the 108,056 NCEI shipborne data were used as a checkpoint to evenly distribute the control points within this study area.

The 72,045 control points were used to evaluate the stability of the GGM estimations over a range of density contrasts by the checkpoint method with GGM in Figure 6. As shown in Figure 6, we selected the range of acceptable density contrasts as 10.0 g/cm^3 and higher from a root mean-square (RMS) difference, a rate of RMS difference, and a correlation coefficient between the control and checkpoints by GGM estimations. At values of 10.0 g/cm^3 and larger, firstly, the correlation coefficient between the control and checkpoints from the GGM estimates levels off at the red curve; secondly, the RMS difference and its rate of RMS difference between the control and checkpoints are stabilized at the blue and green curves, respectively. In this study, the acceptable range of the density contrasts, which minimize the RMS difference from 4.59 m to 0.28 m on the blue one of three curves in the trade-off diagram, was selected at 10.0 g/cm^3 and larger in Figure 6.

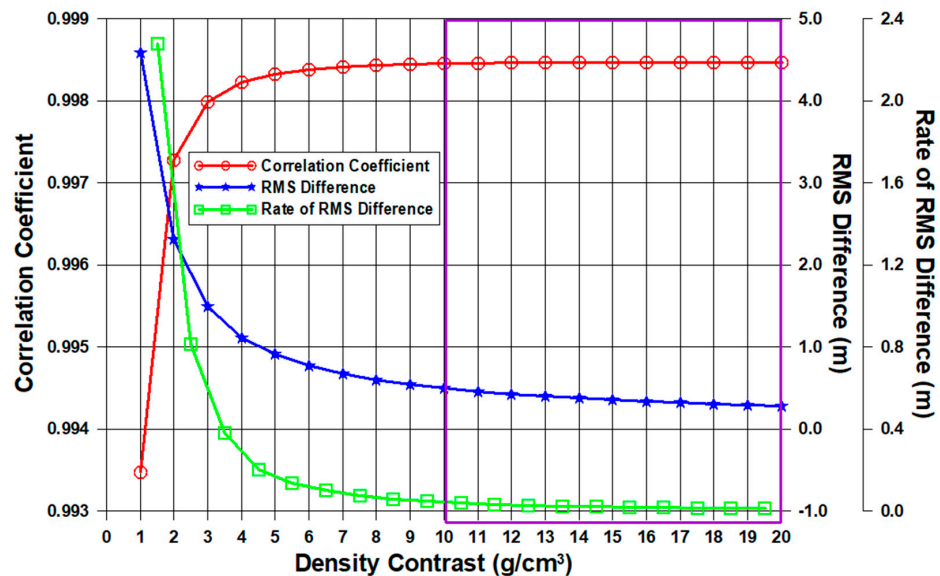


Figure 6. Trade-off diagram for selecting the tuning density contrast range (purple box: 10.0 g/cm^3 and higher) determined from GGM estimations.

The density contrasts were predicted for every level at intervals of 350 m below the sea surface by multiplying the gravity ratio at point i of each downward continued (DWC) level and the sea surface level by 1.03 g/cm^3 . The density contrast of each level was calculated until the levels reached -3756 m , which is the deepest depth. As described in Table 3, the gravity ratio and the predicted density contrast in every DWC level gradually increased with the depth.

Table 3. The density contrast at every level and gravity ratio between the sea surface and the downward continued level in this study area.

DWC Level (m)	−350	−700	−1050	−1400	−1750	−2100	−2450	−2800	−3150	−3500	−3756
Gravity ratio	1.26	1.71	2.20	2.76	3.38	4.09	4.94	6.03	7.57	10.09	13.24
Density contrast (g/cm ³)	1.30	1.76	2.27	2.84	3.48	4.21	5.09	6.21	7.80	10.40	13.63

From Table 3, 13.63 g/cm³ was selected as the predicted density contrast at the deepest depth. The use of the simple Bouguer slab formula in Equation (12) to calculate bathymetry is mitigated by choosing a tuning density contrast of 13.63 g/cm³ between seawater and the ocean bedrock to improve the stability of the GGM predictions.

Because the tuning density contrast is within the acceptable range determined by the checkpoint’s method with GGM, which is denoted as the purple box in Figure 6, the GGM bathymetry predictions were applied to the Yamato basin using a tuning density contrast of 13.63 g/cm³.

The 1 × 1 arc-minute bathymetry models, which are two GGM bathymetry models (GGM 1, GGM 2), NCEI, and ETOPO1 in this study area, are represented in Figure 7. This study generated two bathymetry models, GGM 1 and GGM 2, applied to GGM with a tuning density contrast of 13.63 g/cm³, which was estimated by the downward continuation method, and a density contrast of 1.67 g/cm³ between seawater (1.03 g/cm³) and the ocean bedrock (2.70 g/cm³), respectively, using the depth and gravity anomalies predicted with the exponential GPR model of machine learning. The NCEI gridded model was created using the “surface” routine of Generic Mapping Tools (GMT, <http://soest.hawaii.edu/gmt/>, accessed on 1 May 2024) [33].

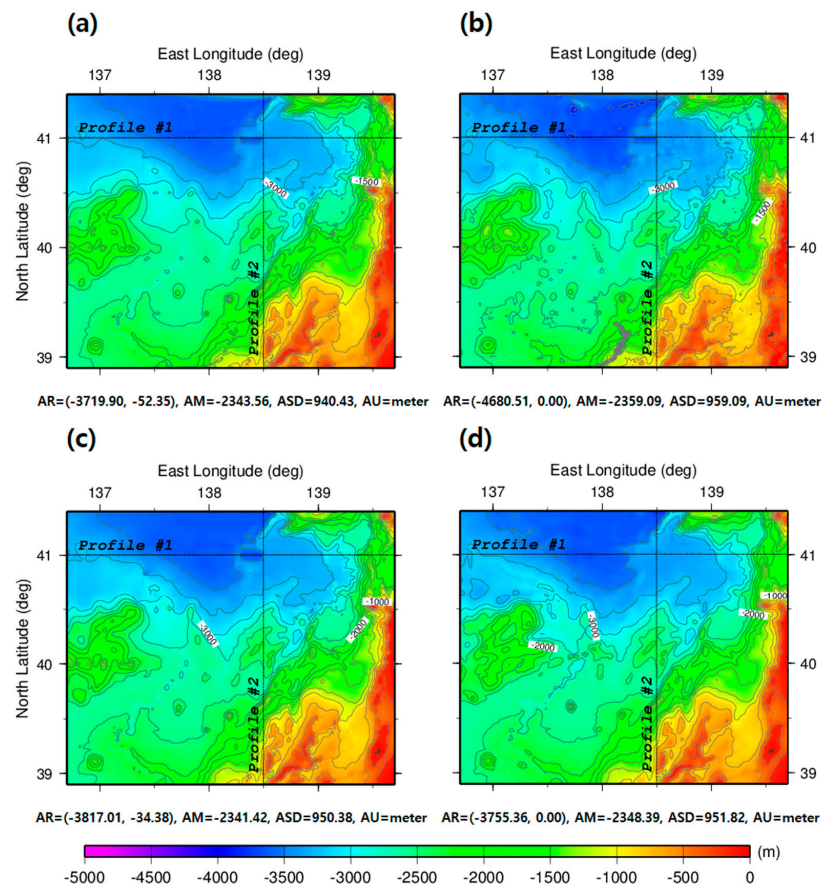


Figure 7. Comparison of bathymetry models: (a) GGM 1, (b) GGM 2, (c) NCEI, and (d) ETOPO1.

Table 4 synthesizes the statistical comparisons of the four bathymetry models. The GGM 1 model in this study area showed correlation coefficients of 0.9948, 0.9962, and 0.9930 with GGM 2, NCEI, and ETOPO1 models, respectively. The GGM 2 model also had a correlation coefficient of 0.9929 and 0.9911 with the NCEI and ETOPO1 models. From the correlation coefficient between the four bathymetry models, GGM 1 and GGM 2 represent a strong correlation with the NCEI gridded model. In the standard deviation in Table 4, the GGM 1 model (940.43 m) is smaller than the three remaining bathymetry models.

Table 4. The statistical comparisons between bathymetry models.

	Min (m)	Max (m)	Mean (m)	STD (m)	CC (Correlation Coefficient)			
					GGM 1	GGM 2	NCEI	ETOPO1
GGM 1	−3719.90	−52.35	−2343.56	940.43	1	0.9948	0.9962	0.9930
GGM 2	−4680.51	0.00	−2359.09	959.09	0.9948	1	0.9929	0.9911
NCEI	−3817.01	−34.38	−2341.42	950.38	0.9962	0.9929	1	0.9957
ETOPO1	−3755.36	0.00	−2348.39	951.82	0.9930	0.9911	0.9957	1

The differences between four bathymetry models (GGM 1, GGM 2, NCEI, and ETOPO1) were computed. Figure 8 presents the maps of point-by-point differences between the models, and Table 5 summarizes their statistics.

Table 5. The statistical comparison of the differences between four bathymetry models.

	Min (m)	Max (m)	Mean (m)	STD (m)
GGM 1—GGM 2	−1023.20	2482.61	15.53	99.08
GGM 1—NCEI	−1434.47	1340.03	−2.14	82.68
GGM 1—ETOPO1	−1093.55	1233.28	4.84	112.56
GGM 2—NCEI	−2825.84	1265.74	−17.67	114.23
GGM 2—ETOPO1	−2832.11	1124.21	−10.70	127.70
NCEI—ETOPO1	−758.07	1045.76	6.97	88.32

In terms of comparing the bathymetry differences, the difference between the GGM 1 and NCEI gridded model exhibited better results with the smallest standard deviation of 82.68 m, as in Table 5. Figure 8a,d,e convey the large differences between GGM 1 and GGM 2, GGM 2 and NCEI, and GGM 2 and ETOPO1 in the southern part of this study area. These large differences were caused by the overestimated GGM 1 bathymetry and underestimated GGM 2 bathymetry in the southern part of this study area, as reflected in Figure 7a,b, respectively. The differences between GGM 1 and GGM 2 in the southern part of this study area ranged from 1024.3 to 2482.6 m, as shown in Figure 8a. The differences between GGM 2 and NCEI and GGM 2 and ETOPO1 in the southern part of this study area ranged from −2832.1 to −1031.8 m, as illustrated in Figure 8d,e.

The histograms of depth difference values between four bathymetry models in Figure 9 indicate that about 95% of the differences between GGM 1 and NCEI were ±85.0 m. Compared to the histogram of depth difference between GGM 1 and NCEI, the other differences are 89.41%, 87.98%, 85.87%, 82.66%, and 89.85% for GGM1—GGM 2, GGM 1—ETOPO1, GGM2—NCEI, GGM2—ETOPO1, and NCEI—ETOPO1, respectively, in the same range.

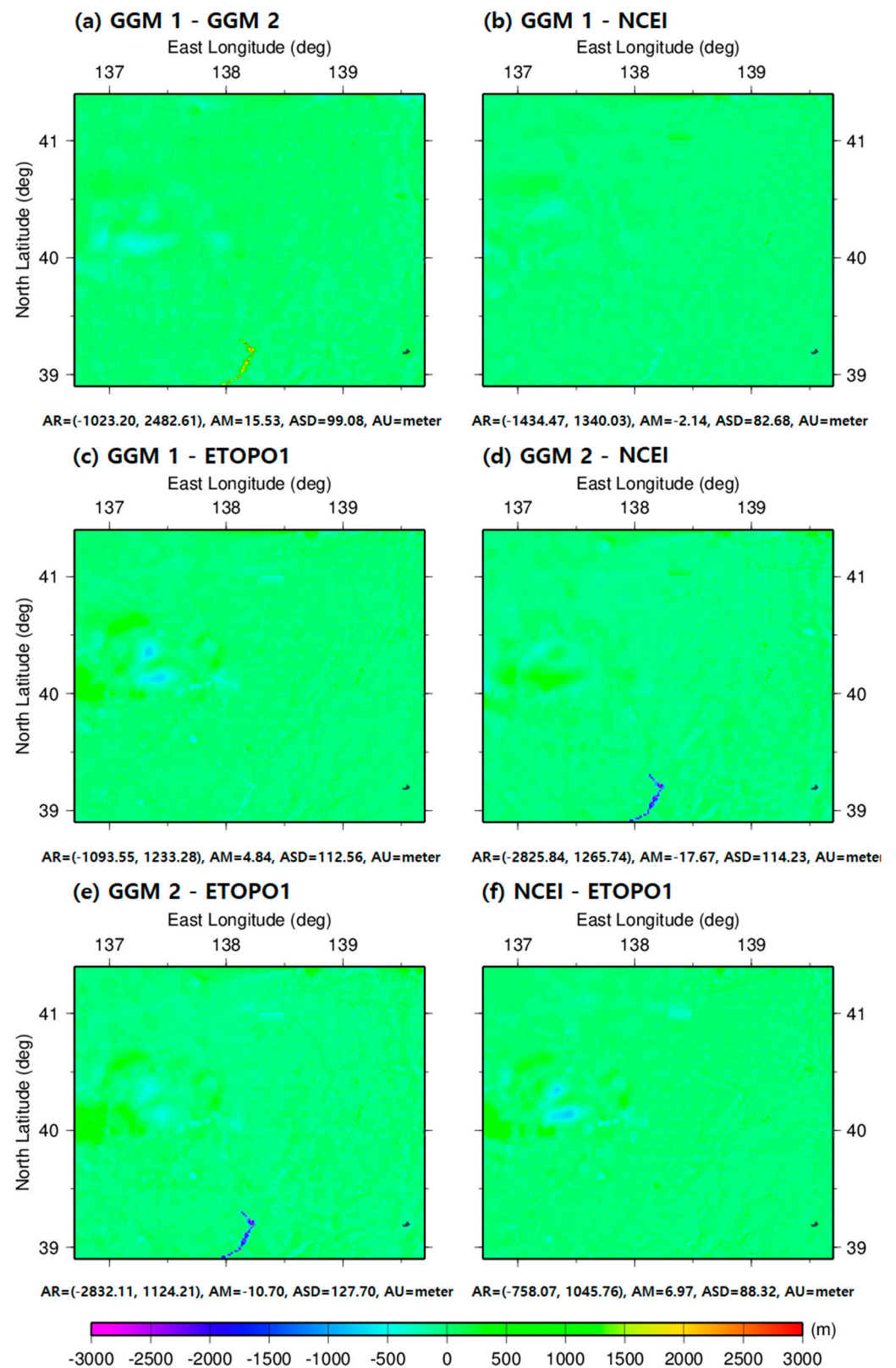


Figure 8. The differences between four bathymetry models (GGM 1, GGM 2, NCEI, and ETOPO1).

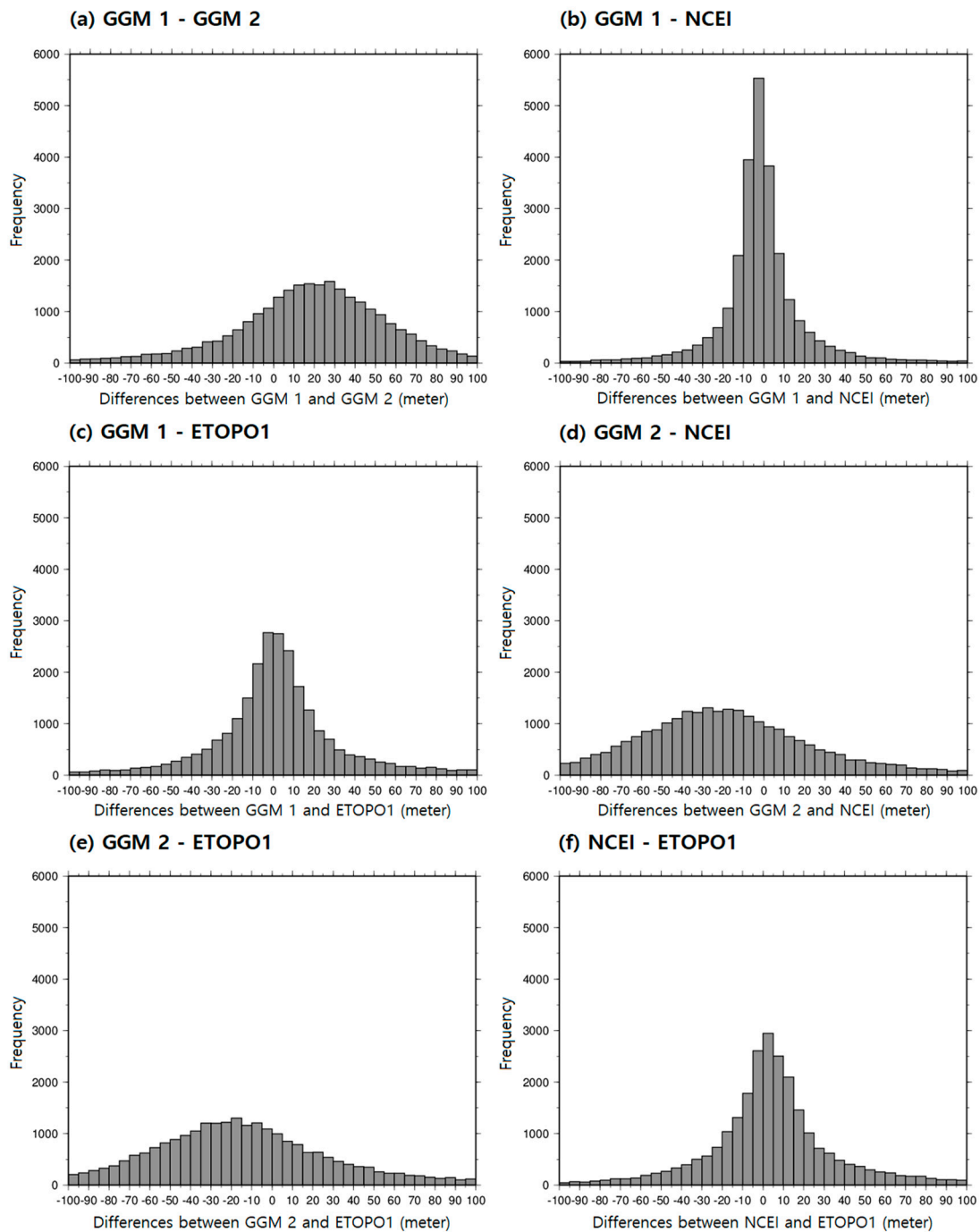


Figure 9. The histograms of six differences between four bathymetry models.

The four bathymetry models were compared to validate the local depth variations in two Profiles: Profile #1 (the east-west direction along 41° N) and Profile #2 (the north-south direction along 138.5° E), shown as black lines in Figure 7. The results are shown in Figure 10. The depths of the four bathymetry models in Profile #1 were strongly correlated, with correlation coefficients between 0.9854 and 0.9997. For Profile #2, the correlation coefficients were also very strongly correlated with correlation coefficients between 0.9923 and 0.9992.

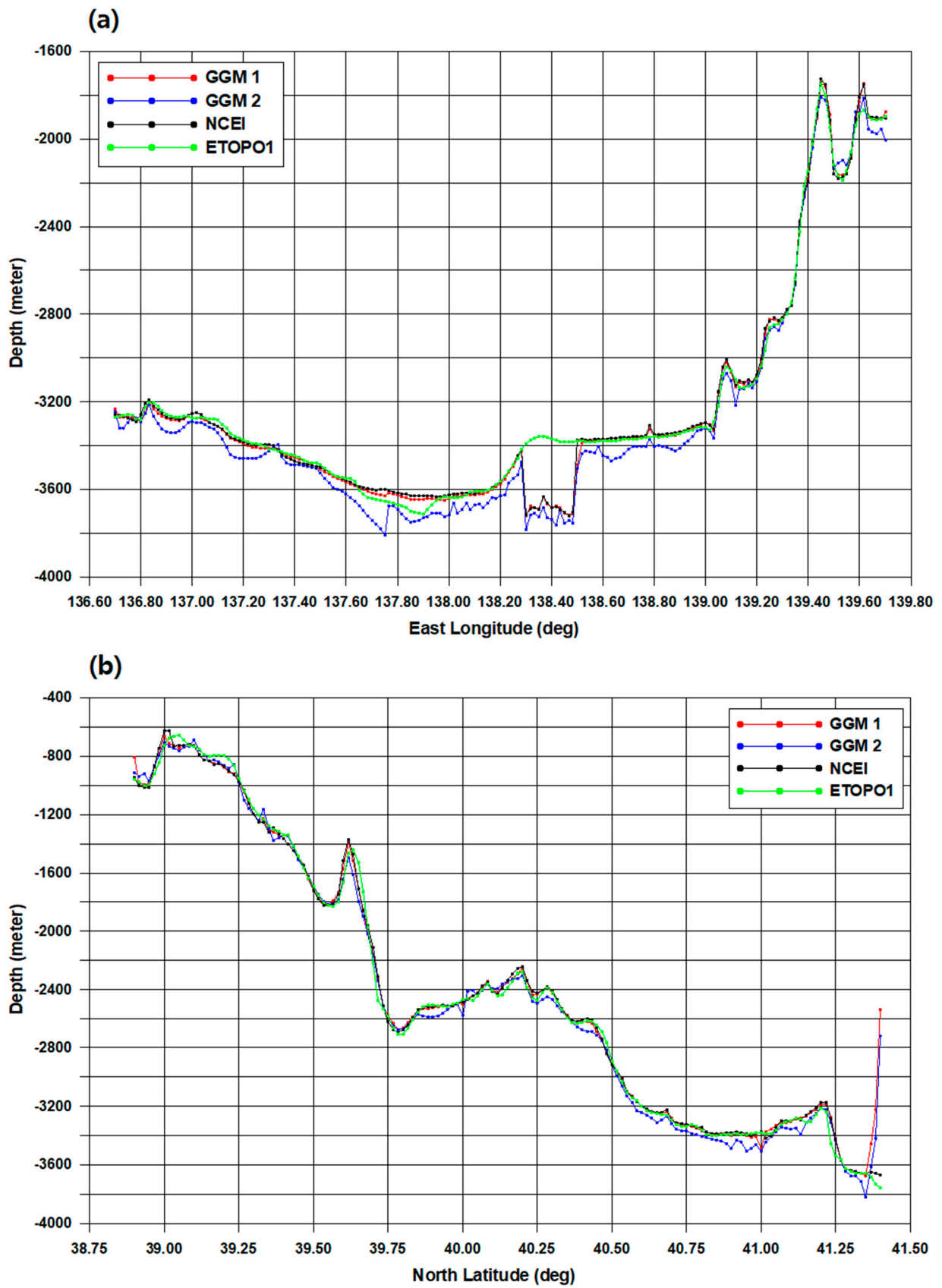


Figure 10. Bathymetry estimate comparisons for Profiles #1 (a) and #2 (b), respectively, as shown in Figure 7.

Table 6 summarizes the statistics of GGM 1, GGM 2, NCEI, and ETOPO1 depths along Profiles #1 and #2. Table 7 presents the statistics of the differences between GGM 1, GGM 2, NCEI, and ETOPO1 depths along Profiles #1 and #2. In the east-west direction along 41° N, the difference between GGM 1 and NCEI had the smallest RMSE value. The difference between NCEI and ETOPO1 had the smallest RMSE value in the north-south direction along 138.5° E.

Table 6. Statistic comparisons between GGM 1, GGM 2, NCEI, and ETOPO1 bathymetry along Profiles #1 and #2.

		Min (m)	Max (m)	Mean (m)	STD (m)
Profile #1	GGM 1	−3719.90	−1742.00	−3239.25	501.13
	GGM 2	−3809.69	−1807.06	−3284.22	513.44
	NCEI	−3720.58	−1726.38	−3232.60	498.77
	ETOPO1	−3714.17	−1747.72	−3221.00	485.69
Profile #2	GGM 1	−3672.62	−663.21	−2381.78	914.27
	GGM 2	−3819.37	−691.77	−2410.15	933.96
	NCEI	−3671.21	−626.30	−2389.71	924.21
	ETOPO1	−3755.36	−655.09	−2395.70	937.36

Table 7. Statistics of the differences between GGM 1, GGM 2, NCEI, and ETOPO1 bathymetry in Profiles #1 and #2.

		Min (m)	Max (m)	Mean (m)	STD (m)	RMSE (m)
Profile #1	GGM 1—GGM 2	−63.02	180.69	44.97	33.64	56.10
	GGM 1—NCEI	−111.86	29.68	−6.65	12.69	14.29
	GGM 1—ETOPO1	−332.00	121.12	−18.26	82.82	84.58
	GGM 2—NCEI	−208.47	73.55	−51.61	38.36	64.24
	GGM 2—ETOPO1	−393.22	88.34	−63.22	87.08	107.41
	NCEI—ETOPO1	−335.87	118.84	−11.61	85.06	85.62
Profile #2	GGM 1—GGM 2	−79.63	191.53	28.37	42.21	50.74
	GGM 1—NCEI	−111.86	1135.87	7.93	102.54	102.51
	GGM 1—ETOPO1	−185.84	1220.02	13.92	117.12	117.56
	GGM 2—NCEI	−162.04	955.38	−20.44	94.42	96.30
	GGM 2—ETOPO1	−271.37	1039.53	−14.44	105.62	106.25
	NCEI—ETOPO1	−182.94	168.59	6.00	45.43	45.68

GGM 2 bathymetry was overall underestimated in the east-west direction along 41° N, as shown in Figure 10a. In particular, the maximum discrepancy of the differences between GGM 2 and ETOPO1 was 393.2 m between 138.20° and 138.60° E. In Figure 10b, the maximum difference between GGM 1 and ETOPO1 reached 1220.0 m between 41.3667° and 41.4000° N due to overestimated GGM 1 bathymetry in the north-south direction along 138.5° E.

In addition, the accuracy of the GGM 1 and GGM 2 bathymetry models predicted using the exponential GPR model of machine learning and GGM was evaluated by interpolation on the 108,056 NCEI shipborne locations, which are represented by the black dots in Figure 2a. Table 8 specifies that the RMSE of the depth differences between GGM 1 and NCEI is smaller than that of the depth differences between GGM 2 and NCEI. Figure 11 shows the depth differences (a) between GGM 1 and NCEI and (b) between GGM 2 and NCEI at 108,056 shipborne depth locations. Consequently, the GGM 1 model using a tuning density contrast of 13.63 g/cm³ in comparison with that using a density contrast of 1.67 g/cm³ shows an improvement of 67.40% in the RMSE at 108,056 shipborne locations of the NCEI. These findings imply that the GGM 1 bathymetry model predicted using the exponential GPR model of machine learning can generate accurate bathymetry around the Yamato basin in the East Sea. The enhancement in accuracy of 82.64 m of GGM 1 in

comparison with GGM 2 concludes that satellite altimetry-derived FAGAs and an optimal machine learning model can effectively estimate accurate bathymetry.

Table 8. Statistics of depth differences on the NCEI shipborne locations between GGM 1 and NCEI and between GGM 2 and NCEI.

	Min (m)	Max (m)	Mean (m)	STD (m)	RMSE (m)
GGM 1	-1372.62	826.89	-3.39	39.82	39.96
GGM 2	-2797.37	882.02	-21.70	120.67	122.60

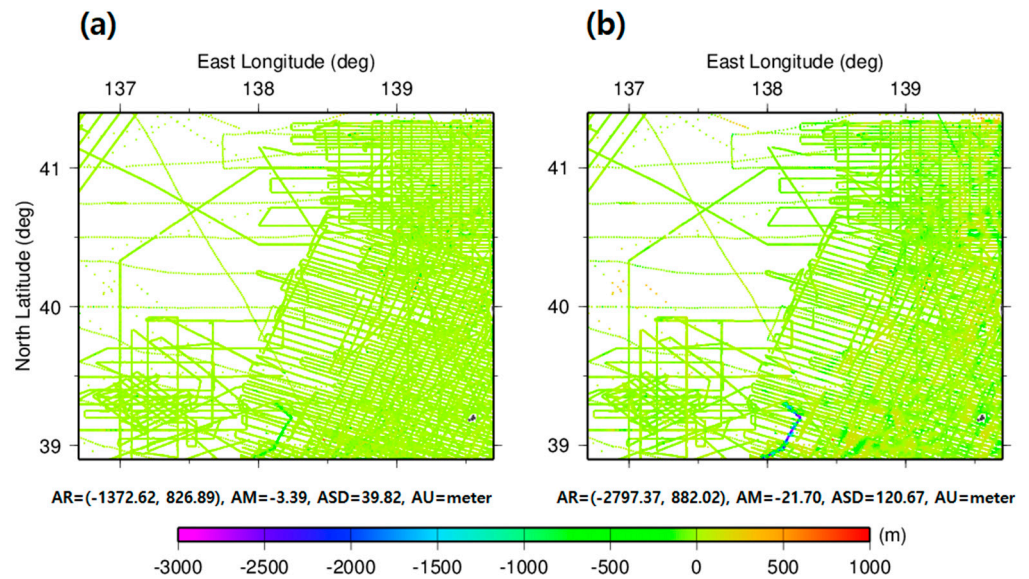


Figure 11. The depth differences in the NCEI shipborne locations (a) between GGM 1 and NCEI and (b) between GGM 2 and NCEI.

Figure 12 graphs the histograms for depth difference values on the NCEI shipborne locations and two models. The histogram for the depth differences between GGM 1 and NCEI displays a narrower distribution of difference values, indicating that there are more precise values around the NCEI depth values. On the other hand, the histogram for the depth differences between GGM 2 and NCEI shows a wider spread, suggesting that the GGM 2 bathymetry model has a higher variability than the depth values.

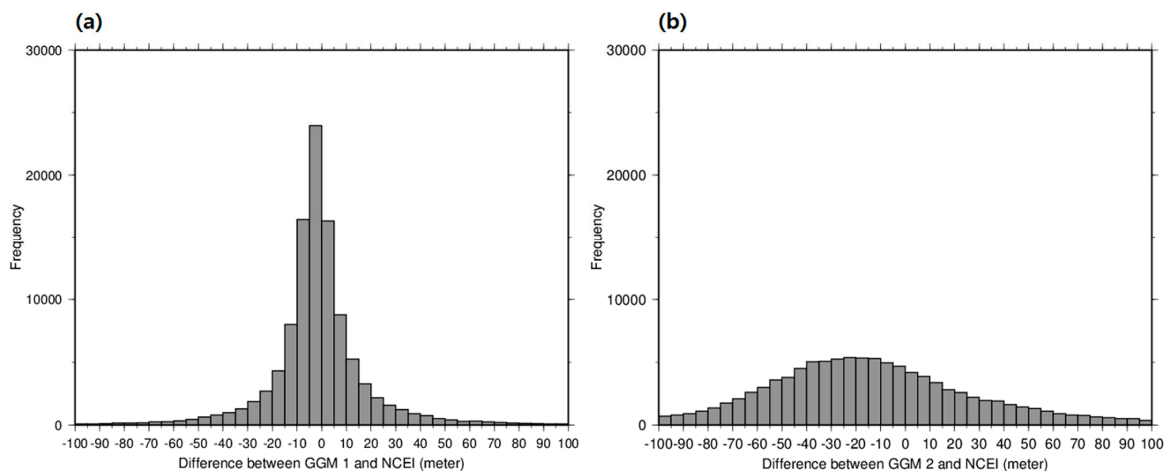


Figure 12. The histograms for the depth differences on the NCEI shipborne locations (a) between GGM 1 and NCEI (b) between GGM 2 and NCEI.

From the histograms of two depth differences from the NCEI shipborne locations and the two competing models presented in Figure 12, it can be gleaned that 91.7% of the depth differences between GGM 1 and NCEI were below 40.0 m, whereas 59.2% of the depth differences between GGM 2 and NCEI were less than 40.0 m. Hence, based on the small differences between the GGM 1 model and the NCEI shipborne depths along the NCEI shipborne locations, the GGM 1 model is considered more suitable than the GGM 2 model for short wavelength bathymetry prediction.

4. Conclusions

Bathymetry estimation was implemented by using satellite altimetry-derived FAGAs and machine learning around the Yamato basin in the East Sea. The depth and gravity anomalies predicted by optimal machine learning performance were applied to improve bathymetry by the gravity-geologic method (GGM) and a tuning density contrast of 13.63 g/cm^3 in this study.

The tuning density of 13.63 g/cm^3 can be more effectively estimated bathymetry by stabilizing GGM estimations by the checkpoint method in the seafloor topography with rugged terrain. The GGM bathymetry predicted by the tuning density contrast (13.63 g/cm^3) improves by 18.66 m over the GGM bathymetry estimated by the theoretical density contrast (1.67 g/cm^3) between seawater and the ocean bedrock, although the tuning density is larger than a geologically reasonable value.

More than 90% of the depth differences between GGM 1 and NCEI on the 108,056 NCEI shipborne locations were below 40.0 m. The results show that the GGM 1 model estimated using a density contrast of 13.63 g/cm^3 compared to the GGM 2 model estimated using a density contrast of 1.67 g/cm^3 improves by 67.40% in the RMSE at 108,056 shipborne locations of the NCEI. These verifications suggest that bathymetry using satellite altimetry-derived FAGAs and machine learning can be effectively improved with higher accuracy.

This study clearly outlines the potential limitations of the approach and identifies future research areas in terms of machine learning. First, since the true values of water depth cannot be measured, it is impossible to assert that a specific model accurately estimates the actual terrain using only RMSE and MAE. Second, as machine learning technology continues to advance in the future, a more accurate estimate of bathymetry can be obtained at any time. The first limitation is difficult to overcome due to the nature of this research, and overcoming the second limitation should be encouraged.

Therefore, future research can be conducted in the direction of overcoming the second limitation. The first is to identify the cause of the difference in machine learning model performance when estimating bathymetry. Once the cause is identified, a better model can be developed or tuned in the future, enabling more accurate bathymetry estimation. The second is to integrate various artificial intelligence techniques. For example, this study and previous studies [9,11,13] show that SVM performs worse than the ensemble model. However, there are cases where the performance of the SVM model has been improved compared to that of the ensemble model through convergence with various artificial intelligence techniques [10]. Therefore, it is expected that these future studies will contribute to estimating more accurate bathymetry.

Author Contributions: K.B.K. conceptualized the original idea and research design and revised the manuscript. J.K. was responsible for this study, conducted data processing, and wrote methodology. H.S.Y. review and editing, supported funding, and administrated this study. All authors have read and agreed to the published version of the manuscript.

Funding: This research was supported by the Basic Science Research Program through the National Research Foundation of Korea (NRF) grant funded by the Korea government (MSIT) (NRF-2021R1A2C2012319). This research was supported by the Basic Science Research Program through the National Research Foundation of Korea (NRF) funded by the Ministry of Education (NRF-2022R1I1A1A01053609).

Institutional Review Board Statement: Not applicable.

Informed Consent Statement: Not applicable.

Data Availability Statement: The original contributions presented in the study are included in the article, further inquiries can be directed to the corresponding author.

Conflicts of Interest: The authors declare no conflict of interest.

References

- Braun, A.; Marquart, G.; Sideris, M.G.; Shum, C.K. How radar altimetry discovered marine geodynamics, In Proceedings of the 15 Years of Progress in Radar Altimetry Symposium, Venice, Italy, 13–18 March 2006.
- Kim, K.B.; Hsiao, Y.-S.; Kim, J.W.; Lee, B.Y.; Kwon, Y.K.; Kim, C.H. Bathymetry enhancement by altimetry-derived gravity anomalies in the East Sea (Sea of Japan). *Mar. Geophys. Res.* **2010**, *31*, 285–298. [[CrossRef](#)]
- Kim, J.W.; von Frese, R.R.B.; Lee, B.Y.; Roman, D.R.; Doh, S.J. Altimetry-derived gravity predictions of bathymetry by gravity-geologic method. *Pure Appl. Geophys.* **2011**, *168*, 815–826. [[CrossRef](#)]
- Roman, D.R. An Integrated Geophysical Investigation of Greenland’s Tectonic History. Ph.D. Dissertation, Ohio State University, Columbus, OH, USA, 1999.
- Kim, K.B.; Lee, C.K. Bathymetry change investigation of the 2011 Tohoku earthquake. *J. Kor. Soc. Surv. Geodesy Photogramm. Cartogr.* **2015**, *33*, 181–192. [[CrossRef](#)]
- Annan, R.F.; Wan, X. Mapping seafloor topography of Gulf of Guinea using an adaptive meshed gravity-geologic method. *Arab. J. Geosci.* **2020**, *23*, 301.
- Yeu, Y.; Yee, J.-J.; Yun, H.S.; Kim, K.B. Evaluation of the accuracy of bathymetry on the nearshore coastlines of western Korea from satellite altimetry, multi-beam, and airborne bathymetric LiDAR. *Sensors* **2018**, *18*, 2926. [[CrossRef](#)] [[PubMed](#)]
- Alevizos, E. A combined machine learning and residual analysis approach for improved retrieval of shallow bathymetry from hyperspectral imagery and sparse ground truth data. *Remote Sens.* **2020**, *12*, 3489. [[CrossRef](#)]
- Tonion, F.; Pirotti, F.; Faina, G.; Paltrinieri, D. A machine learning approach to multispectral satellite derived bathymetry. *ISPRS Ann. Photogramm. Remote Sens. Spat. Inf. Sci.* **2020**, *3*, 565–570.
- Surisetty, V.V.A.K.; Venkateswarlu, C.; Gireesh, B.; Prasad, K.V.S.R.; Sharma, R. On improved nearshore bathymetry estimates from satellites using ensemble and machine learning approached. *Adv. Space Res.* **2021**, *68*, 3342–3364. [[CrossRef](#)]
- Eugenio, F.; Marcello, J.; Mederos-Barrera, A.; Marques, F. High-resolution satellite bathymetry mapping: Regression and machine learning-based approaches. *IEEE Trans. Geosci. Remote Sens.* **2022**, *60*, 5407614. [[CrossRef](#)]
- Ashphaq, M.; Srivastava, P.K.; Mitra, D. Analysis of univariate linear, robust-linear, and non-linear machine learning algorithms for satellite-derived bathymetry in complex coastal terrain. *Reg. Stud. Mar. Sci.* **2022**, *56*, 102678. [[CrossRef](#)]
- Zhou, W.; Tang, Y.; Jing, W.; Li, Y.; Yang, J.; Deng, Y.; Zhang, Y. A comparison of machine learning and empirical approaches for deriving bathymetry from multispectral imagery. *Remote Sens.* **2023**, *15*, 393. [[CrossRef](#)]
- Cheng, J.; Cheng, L.; Chu, S.; Li, J.; Hu, Q.; Ye, L.; Wang, Z.; Chen, H. A comprehensive evaluation of machine learning and classical approaches for spaceborne active-passive fusion bathymetry of coral reefs. *ISPRS Int. J. Geo-Inf.* **2023**, *12*, 381. [[CrossRef](#)]
- Annan, R.F.; Wan, X. Recovering bathymetry of the Gulf of Guinea using altimetry-derived gravity field products combined via convolutional neural network. *Surv. Geophys.* **2022**, *43*, 1541–1561. [[CrossRef](#)]
- Li, Q.; Zhai, Z.; Li, Q.; Wu, L.; Bao, L.; Sun, H. Improved bathymetry in the South China Sea from multisource gravity field elements using fully connected neural network. *J. Mar. Sci. Eng.* **2023**, *11*, 1345. [[CrossRef](#)]
- Kim, K.B.; Kim, J.S.; Yun, H.S. Bathymetry estimation using machine learning in the Ulleung basin in the East Sea. *Sens. Mater.* **2023**, *35*, 3351–3362. [[CrossRef](#)]
- Amante, C.; Eakins, B.W. ETOPO1 1 Arc-Minute Global Relief Model: Procedures, data sources and analysis. In *NOAA Technical Memorandum NESDIS NGDC-24*; National Geophysical Data Center: Boulder, CO, USA, 2009.
- Jolivet, L.; Tamaki, K.; Fournier, M. Japan Sea, opening history and mechanism: A synthesis. *J. Geophys. Res.* **1994**, *99*, 22237–22259. [[CrossRef](#)]
- Sandwell, D.T.; Müller, R.D.; Smith, W.H.F.; Garcia, E.; Francis, R. New global marine gravity model from CryoSat-2 and Jason-1 reveals buried tectonic structure. *Science* **2014**, *346*, 65–67. [[CrossRef](#)]
- Dickens, K.; Armstrong, A. Application of machine learning in satellite derived bathymetry and coastline detection. *SMU Data Sci. Rev.* **2019**, *2*, 4.
- Mountrakis, G.; Im, J.; Ogole, C. Support vector machines in remote sensing: A review. *ISPRS J. Photogramm. Remote Sens.* **2011**, *66*, 247–259. [[CrossRef](#)]
- Cortes, C.; Vapnik, V. Support-vector networks. *Mach. Learn.* **1995**, *20*, 273–297. [[CrossRef](#)]
- Breiman, L. Random forests. *Mach. Learn.* **2001**, *45*, 5–32. [[CrossRef](#)]
- Prasad, A.M.; Iverson, L.R.; Liaw, A. Newer classification and regression tree techniques: Bagging and random forests for ecological prediction. *Ecosystems* **2006**, *9*, 181–199. [[CrossRef](#)]
- Chen, T.; Guestrin, C. XGBoost: A scalable tree boosting system. In Proceedings of the 22nd ACM SIGKDD International Conference on Knowledge Discovery and Data Mining, San Francisco, CA, USA, 13–17 August 2016; pp. 785–794.
- Kulkarni, V.Y.; Sinha, P.K. Random forest classifiers: A survey and future research directions. *Int. J. Adv. Comput.* **2013**, *36*, 1144–1153.

28. Wang, J. An intuitive tutorial to Gaussian processes regression. *Comput. Sci. Eng.* **2023**, *25*, 4–11. [[CrossRef](#)]
29. Murphy, K.P. *Machine Learning: A Probabilistic Perspective*; MIT Press: Cambridge, MA, USA, 2012.
30. Rasmussen, C.E.; Williams, K.I. *Gaussian Processes for Machine Learning*; MIT Press: Cambridge, MA, USA, 2006.
31. Parker, R.L. Understanding inverse theory. *Annu. Rev. Earth Planet. Sci.* **1977**, *5*, 35–64. [[CrossRef](#)]
32. Strykowski, G.; Boschetti, F.; Papp, G. Estimation of the mass density contrast and the 3D geometrical shape of the source bodies in the Yilgarn area, Eastern Goldfields, Western Australia. *J. Geodyn.* **2005**, *39*, 444–460. [[CrossRef](#)]
33. Wessel, P.; Smith, W.H.F.; Scharroo, R.; Luis, J.; Wobbe, F. Generic Mapping Tools: Improved version released. *EOS Trans. Am. Geophys. Union* **2013**, *94*, 409–410. [[CrossRef](#)]

Disclaimer/Publisher’s Note: The statements, opinions and data contained in all publications are solely those of the individual author(s) and contributor(s) and not of MDPI and/or the editor(s). MDPI and/or the editor(s) disclaim responsibility for any injury to people or property resulting from any ideas, methods, instructions or products referred to in the content.